A fatigue lifetime prediction model applicable to porous sintered Ag nanoparticles

Indexed by:
Web of Science Group

Zhongqing Zhang[a,b], Guicui Fu[a], Bo Wan[a,*], Yutai Su[c]

[a] School of Reliability and Systems Engineering, Beihang University, China
[b] QianYuan National Laboratory, China
[c] Chongqing Innovation Center, Northwestern Polytechnical University, China

Highlights

- A new fatigue lifetime prediction model is developed for sintered Ag nanoparticles.
- This model considers damage slip accumulation, stiffness and strength fatigue degradation.
- A low-cost method for estimating key model parameters of prediction model is proposed.
- This model provides a solution that balances model complexity and engineering convenience.
- This paper provides a novel perspective for the reliability analysis of porous structures.

Abstract

Sintered silver nanoparticles (AgNPs) are widely used in the electronic packaging of high-power chips, yet their random internal porous structure is prone to fatigue degradation. In this study, a new cyclic cohesive zone model (CCZM) is proposed for predicting the fatigue lifetime of sintered AgNPs. This model not only considers the cumulative effect of damage slip during cyclic loading but also realizes simultaneous stiffness and strength fatigue degradation under low-stress loading. In addition, to improve the usability of the model, a low-cost estimation method of the model's key parameters and the corresponding VUMAT user subroutines are proposed. Based on this, cyclic tensile tests on Sintered specimens confirm the occurrence of damage slip within the porous AgNPs structure. The predictive performance of the model and the sensitivity of its characteristic parameters are also thoroughly analyzed and discussed. The new CCZM provides a solution that balances modeling complexity and engineering convenience for the reliability assessment of porous structures.

Keywords

sintered silver nanoparticles, damage slip, new cyclic cohesive zone model, fatigue lifetime prediction

1. Introduction

Sintered silver nanoparticles (AgNPs) are favored as packaging materials for high-power chips due to their exceptional thermal conductivity [1]. Sintered AgNPs provide electrical interconnections and structural support between the chip and the substrate. Nonetheless, they possess complex random porous structures [2], and when subjected to long-term service in complex alternating thermal and mechanical environments, they are prone to fatigue degradation [3], rendering a weak point in the interconnection package structure [4], [5]. Therefore, it is necessary to focus on their reliability and evaluate their service lifetime, to promote the reliable application of sintered AgNPs in high-power semiconductor devices.

Conducting reliability assessments from the perspective of lifetime prediction has seen substantial development in recent years [6], [7], [8], [9]. In comparison to time-consuming and costly reliability tests, theoretical analyses and predictive models have become more favored among researchers, as they provide a more intuitive and rapid understanding of product

(*) Corresponding author.
E-mail addresses: Z. Zhang (ORCID: 0000-0002-3933-1929) beckeet@126.com, G. Fu (ORCID: 0000-0001-6295-3454) fuguicui@buaa.edu.cn, B. Wan (ORCID: 0000-0003-1460-3614) wanbo@buaa.edu.cn, Y. Su (ORCID: 0000-0001-7756-2560) suyutai@nwpu.edu.cn

reliability [10]. For example, traditional S-N curves [11] and the Paris model [12] provide rough estimates of fatigue lifetime and reliability. The Physics of Failure (PoF) [13], a semi-mechanistic and semi-empirical predictive model, further enhances the effectiveness of these assessments. Moreover, prediction methods based solely on degradation-driven data rely on earlier accelerated degradation tests and historical monitoring data [14], [15]. Usually, this kind of reliability data is very rare, which somewhat restricts its widespread application. Currently, numerical simulation methods, exemplified by finite element analysis, are more popular in practical applications due to their high predictive accuracy and visualization capabilities [16]. The cohesive zone model (CZM) is one of the more effective numerical simulation methods, developed based on damage and fracture mechanics theory. It uses Traction-Separation (T-S) curves to describe the mechanical response of the interconnection structure, offering a more intuitive and concise approach compared to other methods. Over the past few years, CZM has been widely applied and shows great potential in predicting the lifetime of porous structures [17].

The cyclic cohesive zone model (CCZM) is developed based on CZM [18]. The primary focus of CCZM is to establish a link between fatigue damage and performance degradation. The most direct means is the stiffness or strength degradation, as shown in Fig. 1(a). Choi et al. [19] proposed a CCZM model based on stiffness degradation. Damage is calculated when the maximum traction stress threshold is surpassed. This model effectively simulates crack propagation in composite materials [20]. Xun et al. [21] introduced a strength degradation-based CCZM, which has been widely applied in geotechnical engineering to model fatigue-induced material strength reduction. Roe-Siegmund et al. [22] presented a highly regarded CCZM that accounts for both simultaneous stiffness and strength degradation [23]. This model ingeniously formulates a nonlinear damage constitutive relationship using an exponential functional form [24], as shown in Fig. 1(b). Building on this concept, an elastic-plastic damage CCZM with a potential function form has also been developed [25], [26]. However, the aforementioned CCZMs all assume that the unloading path returns directly to the origin and do not consider the unique degradation behavior of porous structures during the fatigue stage. The limitations of unloading along the origin in the CCZM have been reported [27], [28]. Moreover, most CCZMs commence damage calculations solely upon reaching damage initiation stress (maximum traction), which not only overlooks fatigue damage occurring under low-stress conditions but may also lead to unrealistic lifetime predictions for sintered AgNPs.
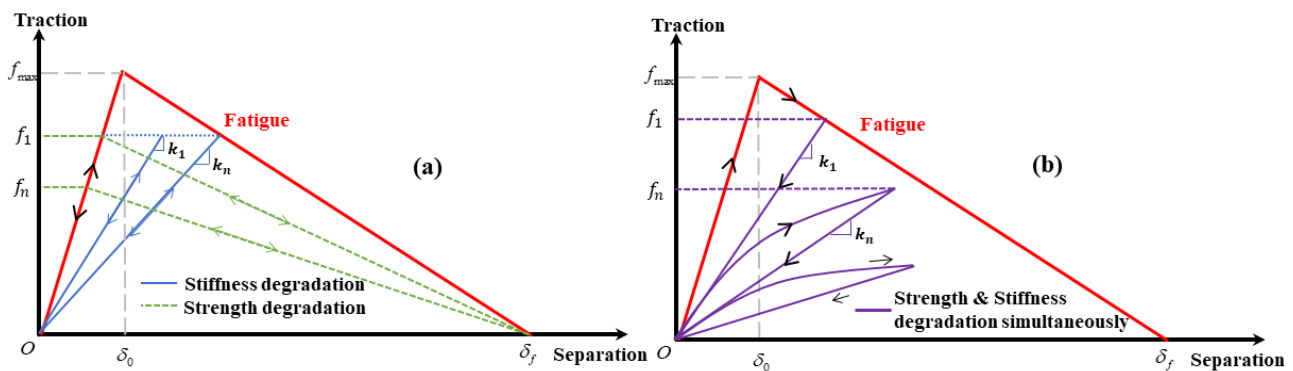

Fig. 1. Common CCZMs for fatigue lifetime prediction. (a) Stiffness or strength degradation. (b) Both stiffness and strength degradation simultaneously.

Therefore, a new CCZM is proposed for considering the unique degradation behavior and predicting the fatigue lifetime of porous sintered AgNPs. This model not only does not ignore the low-stress damage but also considers the damage slip accumulation. The findings of this paper will aid designers in their initial reliability design efforts as well as users in conducting prognostic analyses [29]. In the rest of this paper, Sec.2 introduces the modeling background. Sec.3 introduces the constitutive relationships, damage calculation formulas, and application methods of the new CCZM. Sec.4 conducts model validation. Sec.5 analyzes the sensitivity of the model's characteristic parameters. Sec.6 summarizes the findings of the paper.

2. Model Building Background

Due to the particularity of the low-temperature sintering process, sintered AgNPs are a typical random porous material. During the cyclic loading process, tiny cracks initiate and propagate within AgNPs, leading to microscopic metal bond breakage and internal dislocation slip motion [30]. Typically, this minor internal structural damage is both unnoticeable and irreversible. The irreversibility of dislocation slip in microstructures has been extensively discussed by Hael Mughrabi et al. [31] Although the damage has already occurred, the material tends to revert to its initial position after unloading [32], a phenomenon referred to as "virtual connection.". Upon stress reloading, the virtual connection area rapidly disengages, providing a potential path for crack propagation. In addition, when a void is present in front of a damaged area, a broader slip is likely to occur. This phenomenon is termed "damage slip," as depicted in Fig. 2
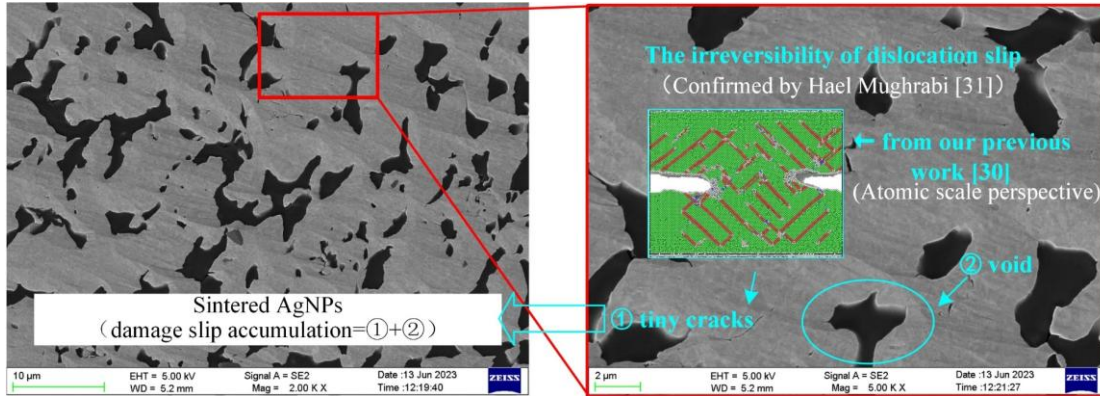

Fig. 2. Damage slip behavior of sintered AgNPs.

Conventional CCZMs are developed for composite delamination and colloidal degradation and are not fully applicable to describe the fatigue degradation of porous materials. Under cyclic loading conditions, the sintered body's damaged area diminishes resistance to crack propagation, leading to variations in displacement on the T-S curve under identical stress conditions. However, most CCZMs that unload and reload from the origin fail to capture this damage slip phenomenon. Furthermore, previous damage initiation conditions required the load to reach the maximum traction force or for the opening displacement to exceed the damage initiation threshold, which overlooked minor damage at low stress levels and contradicted the concept of cyclic irreversibility [31]. Therefore, it is imperative to develop a new CCZM to address these limitations.

3. New Cyclic Cohesive Zone Model
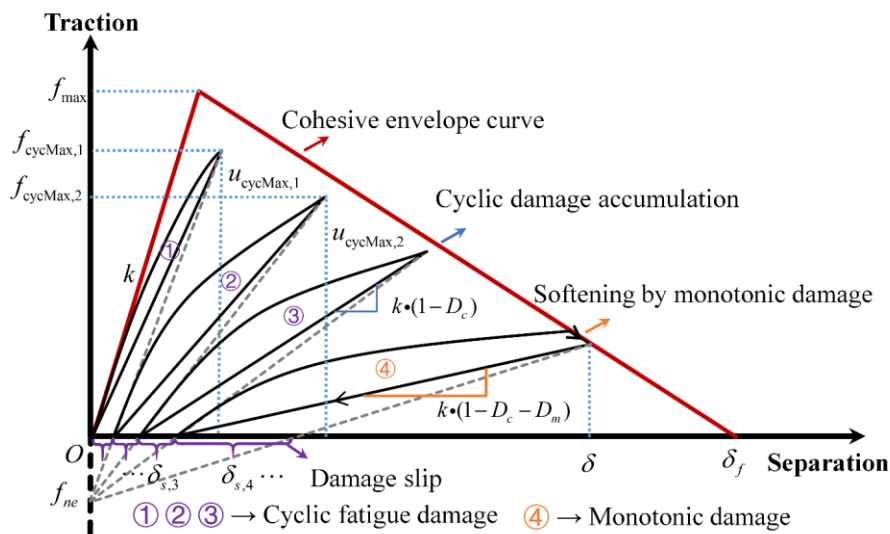
3.1. Model description

Fig. 3. Schematic diagram of the new CCZM constitutive model.

The new CCZM consists of four parts: the envelope curve, damage slip, cyclic fatigue damage stage, and monotonic softening stage. When the cohesive element is subjected to an external load that does not exceed the envelope curve, it enters the fatigue damage stage, where stiffness and strength begin to degrade, with synchronous damage slip occurring. Upon entering the unloading stage, it maintains the stiffness value prior to unloading and returns to the starting position without damage. Upon entering the reloading stage, it continues to progress from the position of accumulated damage slip, and fatigue damage continues to increase. Once the load reaches or exceeds the envelope curve, the model transitions to the monotonic softening stage, where the material's softening behavior is same as traditional CZM's damage behavior. The failure criterion of the new model is defined as either the damage accumulation reaching a value of 1 or the damage slip accumulation reaching the failure displacement of the envelope curve. In summary, the new constitutive model has the following three characteristics:

In summary, the new CCZM has the following three characteristics:

1) Minor damage under low stress conditions is accounted for.

2) Fatigue damage leads to simultaneous degradation of both stiffness and strength.

3) The cumulative effect of damage slip during cyclic loading is taken into consideration.

Noted, the envelope curve of the new CCZM is not limited to a bilinear form. Still, it can adopt an exponential or trapezoidal form, according to the actual service behavior of the material. Moreover, this study assumes that the constitutive model applies uniformly to both the normal and tangential directions of the cohesive element, and will not separately distinguish these directions in the following expressions.

3.2. Damage calculation

Fig. 3 consists of a linear elastic phase in the ascending region, as shown in Eq. (1), and a plastic separation phase in the descending region, as shown in Eq. (2). When the traction stress does not exceed the T-S envelope curve, fatigue damage increment is calculated by Eq. (3). If the traction stress exceeds the envelope curve, the CCZM enters the monotonic damage

stage, with stiffness softening becoming apparent. Further loading at this stage drives separation displacement along the envelope curve, as shown in Fig. 3, stage 4, with monotonic damage increment in the softening phase described by Eq. (4).

$$f = k \cdot \delta \qquad (1)$$

where f is traction stress, k is stiffness, δ is separation displacement.

$$\delta_f = 2G/f_{max} \qquad (2)$$

where δ_f is failure separation displacement, f_{max} is the maximum traction stress. G is the energy release rate, commonly referred to as fracture energy

$$\dot{D}_c = a \frac{\langle \dot{\delta} \rangle}{d_\Sigma} \left[\frac{f}{f_{max}} - C_f \right] \qquad (3)$$

Where $\dot{D}_c$ is the cyclic fatigue damage increment, $\dot{\delta}$ is the displacement increment, $d_\Sigma = n\delta_0 = n \cdot (f_{max}/k)$ is the damage scaling factor, usually n times of δ_0. f is the traction stress at the current moment, f_{max} is the maximum traction stress, C_f and a are constants.

$$\dot{D}_m = \frac{\delta_0 \delta_f \langle \dot{\delta} \rangle}{\delta^2 (\delta_f - \delta_0)} \qquad (4)$$

Where $\dot{D}_m$ is the monotonic damage increment. δ is the current moment displacement.

Damage calculations are omitted during the unloading stage. The new CCZM's total damage and the corresponding cohesive element stress are presented in Eq. (5) and Eq. (6), respectively.

$$D = \int \left(\dot{D}_c + \dot{D}_m \right) dt = D_c + D_m \qquad (5)$$
$$f_* = k \cdot (1 - D) \cdot \delta_* \qquad (6)$$

Where f_* and δ_* are the current traction stress and current separation displacement.

3.3. Damage slip accumulation calculation

The damage slip value is defined as the intersection of the maximum stress loading point pointing to a non-zero negative phase f_{ne} and the horizontal axis within a cycle, as shown in Eq. (7). This slip displacement is not a fixed value and increases with rising damage.

$$\delta_{s,i} = \frac{-f_{ne} \cdot u_{cycMax,i}}{f_{cycMax,i} - f_{ne}} - \delta_{s,i-1} \quad f_{ne} = -ne \cdot f_{max} \qquad (7)$$

In the i-th cycle, where $\delta_{s,i}$ is the damage slip, $\delta_{s,0}$ is the initial slip value, $u_{cycMax,i}$ is maximum separation, $f_{cycMax,i}$ is maximum traction stress, f_{ne} is the non-zero negative phase point when unloading. The cumulative total amount of damage slip is shown in Eq. (8)

$$\delta_{s,all} = \sum_{i=1}^{n} \delta_{s,i} \qquad (8)$$

Where $\delta_{s,all}$ is the total damage slip, n is the cycle count.
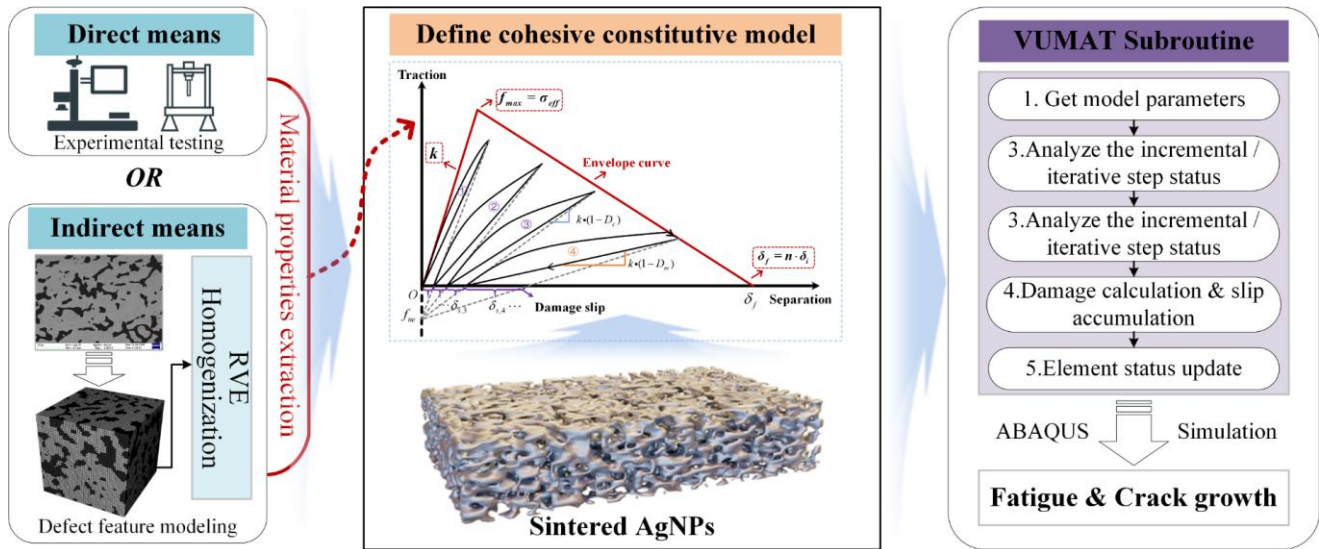
3.4. How to use this model

Fig. 4. Main steps in the implementation process of the new CCZM.

Fig. 4 outlines the main steps in the implementation process of the new CCZM, including material parameter extraction, key parameter determination, VUMAT subroutine development, and numerical simulation. The accuracy of model key parameters critically influences the predictive effect. Several methods exist for obtaining the CCZM envelope curve, with material performance testing being the most straightforward.

However, certain situations are impractical, necessitating a simple, fast, cost-effective method for evaluating material performance. To address this, we propose a 3D Gaussian Random Field (GRF) defect modeling method, depicted in Fig. 5, combined with RVE homogenization techniques to evaluate the material properties of sintered AgNPs, and derive the key parameters of the new CCZM.
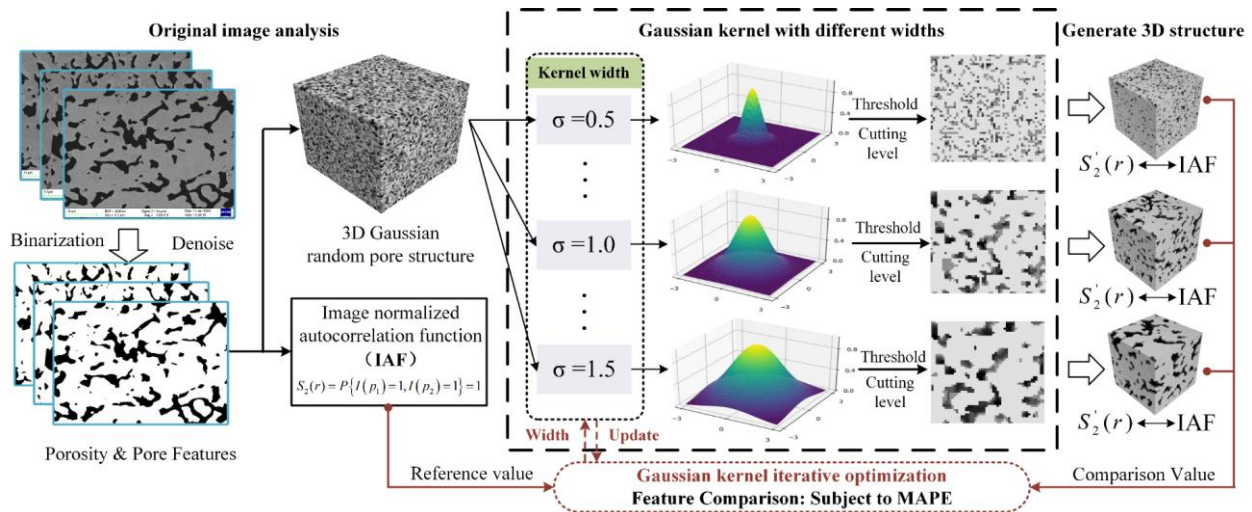

Fig. 5. The defect feature modeling process of sintered AgNPs based on 3D GRF.

Fig. 5 shows the defect feature modeling process of sintered AgNPs, including binarization and noise reduction of SEM images, pore feature extraction, 3D model spatial discrete point distribution, and Gaussian kernel iterative optimization. A more detailed theoretical analysis can be found in our previous work

[33]. This paper quantitatively analyzes defect characteristics using the Image Autocorrelation Function (IAF) and evaluates the similarity between the real and generated structures based on this analysis. For a 2D image, the IAF uses Eq. (9) to measure the correlation between pixels at different positions.

$$R(x,y) = I(x,y) \otimes I(x,y) = \frac{1}{MN}\sum_{m=0}^{M-1}\sum_{n=0}^{N-1} I(m,n) \cdot I(x-m, y-n) \qquad (9)$$

Where (x,y) are pixels' coordinates. (m,n) are target pixels. Generally, the Fourier-transformed convolution theorem can be used to simplify computational processes, as shown in Eq. (10).

$$R(x,y) = I(x,y) \otimes I(x,y) = FT^{-1}\{|FT\{I(x,y)\}|^2\} \qquad (10)$$

Where FT and FT^{-1} represent the Fourier transform and inverse Fourier transform, respectively.

Another key step shown in Fig. 5 involves optimizing the width of the Gaussian kernel to ensure that the defect structure generated by the 3D GRF aligns with the real sintered AgNPs structure observed in the SEM. The optimization target is to minimize the mean absolute percentage error (MAPE) of the normalized IAF between the real structure and the generated RVE structure. The formula for MAPE is provided in Eq. (11).

$$MAPE = \frac{1}{n}\sum_{i=1}^{n}\left|\frac{R(r_i) - R'(r_i)}{R(r_i)}\right|, \quad r_i = \sqrt{(x_i - x'_i)^2 + (y_i - y'_i)^2} \qquad (11)$$

Where $R(r_i)$ and $R'(r_i)$ are the normalized IAF corresponding to the i-th pixel distance in the real structure and the generated structure, respectively.

Material's macroscopic properties depend on the microstructure's arrangement. The concept of predicting material performance based on RVE was first proposed by Hill et al. [34]. It is defined as the smallest volume element that can accurately represent the average constitutive properties of the macroscopic model. Then, Periodic boundary conditions (PBC) need to be applied to the RVE model to simulate the deformation of the surrounding material, while ensuring stress and displacement continuity [35]. Commercial finite element software uses Python scripts to apply constraint equations on nodal degrees of freedom (DoF) for implementing PBCs [36]. Eq. (12) displays the displacement field on the RVE boundary.

$$U_i(x,y,z) = \bar{\varepsilon}_{ik}u_k(x,y,z) + U_i^*(x,y,z) \qquad (12)$$

Where $\bar{\varepsilon}_{ik}$ is the average strain. $u_k(x,y,z)$ are boundary coordinates. $U_i^*(x,y,z)$ is displacement correction of PBC. Eq. (13) is the displacement formula of the two symmetrical boundaries of RVE.

$$U_i^{j+}(x,y,z) = \bar{\varepsilon}_{ik}u_k^{j+}(x,y,z) + U_i^*(x,y,z) \\ U_i^{j-}(x,y,z) = \bar{\varepsilon}_{ik}u_k^{j-}(x,y,z) + U_i^*(x,y,z) \qquad (13)$$

Subtract the above formulas to form a general expression, as follows:

$$U_i^{j+} - U_i^{j-} = \bar{\varepsilon}_{ik}(u_k^{j+} - u_k^{j-}) = \bar{\varepsilon}_{ik}\Delta u_k^j \qquad (14)$$

The elastic-plastic behavior of the material can be predicted using the RVE homogenization method. Furthermore, a fast calculation formula proposed by Wang et al. [37]. can be used to determine one of the key parameters of the new CCZM: the maximum traction force, as shown in Eq. (15).

$$f_{max} = \sigma_{eff} = \frac{4}{3}\sigma_f \; or \; \frac{\sigma_f}{1-d} \qquad (15)$$

Where σ_f is the stress on the material as it enters the rapid damage region. d is a damage scalar, which is related to the critical pore volume ratio and usually takes values in the range of 0.26-0.3 [37]. σ_{eff} is critical stress. f_{max} is the maximum traction stress.

Fracture energy, another key parameter, can be represented by the enclosed area of the T-S curve, as shown in Eq. (16). It represents the energy required for the instability propagation of cohesive elements [24], [38].

$$G = \frac{\delta_{df} \cdot f_{max}}{2} = \frac{n\delta_{di} \cdot f_{max}}{2} = \frac{nf_{max}^2}{2k} \qquad (16)$$

For the bilinear CCZM, δ_{df} is considered to be n times of δ_{di}. n is usually between 10 to 20. Referring to the CZM measurement test on sintered AgNPs by Dai et al. [39], n is recommended to be 15.

Once the shape of the new CCZM is determined, it can be integrated into the ABAQUS explicit solver through the VUMAT subroutine. This process involves five main steps, as shown in Fig. 4. Firstly, obtain the basic parameters (e.g., stiffness, maximum traction stress, fracture energy, etc.) of the cohesive element and the transfer variables (e.g., total damage value, cumulative damage slip, system status, etc.) of the VUMAT subroutine. Secondly, calculate the try displacement at the current moment. Thirdly, determine the system status (e.g., continuous rising stage, unloading stage, and reloading stage) and update displacement value accordingly. Fourthly, calculate fatigue or monotonic damage. Finally, update the cohesive element's stress and state, including decisions on element deletion, as detailed in Eq. (17). The VUMAT subroutine will be called in every numerical increment and cycle until loading completion or model failure.

$$S_{element} = \begin{cases} Damage \geq 1 \\ uNew \geq \delta_f \end{cases} \Rightarrow S_{element} = 0.0 \\ else \qquad \Rightarrow S_{element} = 1.0 \qquad (17)$$

Where $S_{element}$ is the cohesive element's state. $S_{element}=0.0$ means the element fails.
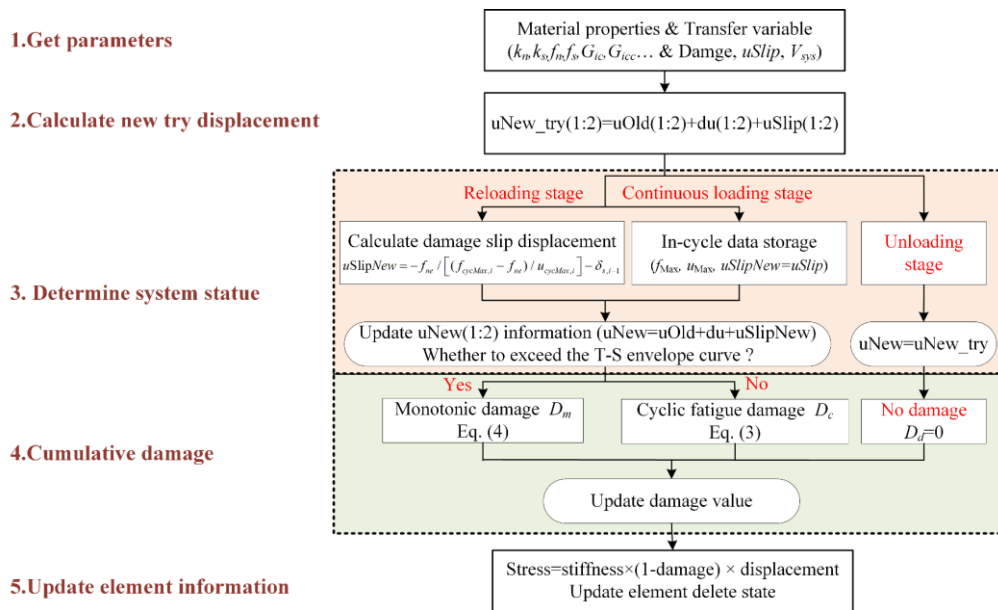
Fig. 6. The calculation process of the new CCZM in ABAQUS explicit solver.

4. Implementation and verification

4.1. Preparation and observation of sintered specimens

In this work, commercial AgNPs paste with a main diameter of 250nm was used, and the specimen was prepared using a 350PC automatic dispensing machine. A 1mm notch was pre-set in the specimen to fracture easily at the center during testing. The preparation process and sintering conditions are shown in Fig. 7. Afterward, the specimen was surface-ion polished using the Fischione Model 1061 mill, with SEM images captured via a ZEISS Merlin.
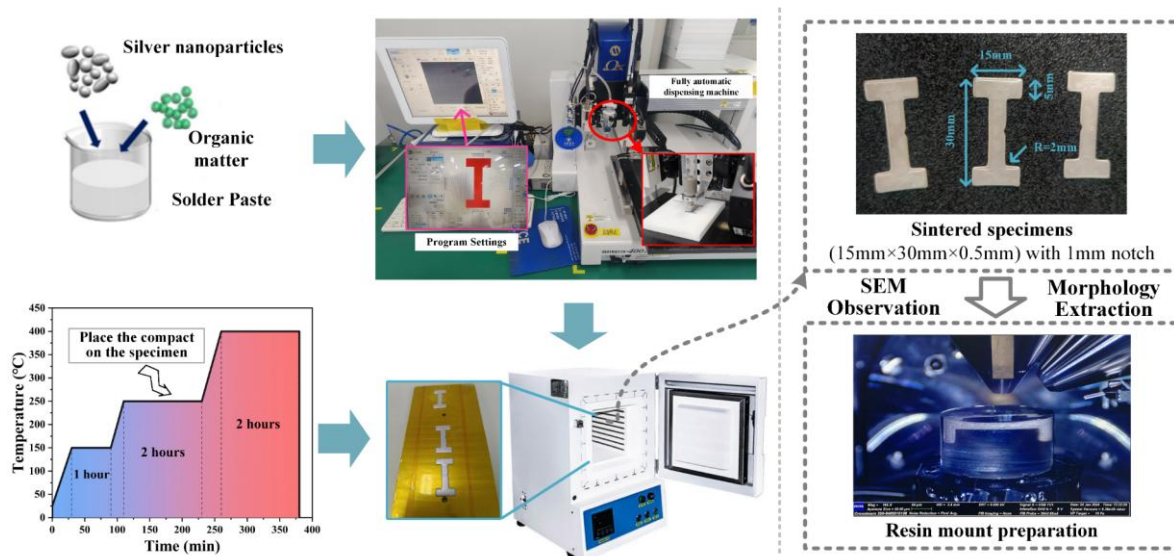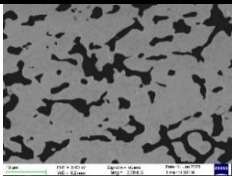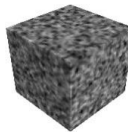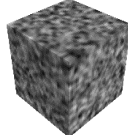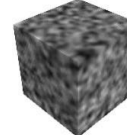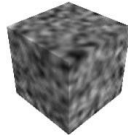

Fig. 7. The preparation process and sintering conditions.

4.2. RVE generation & cohesive element parameter calculation

Based on real microstructure images, the 3D RVE structure of sintered AgNPs is reconstructed using the 3D GRF defect modeling method established in Sec. 3.4. The RVEs generated by different Gaussian kernel widths and their respective IAFs are shown in Table 1 and Fig. 8. As shown in Fig. 8(b), when the Gaussian kernel width is 2.813, the defect feature structure generated based on 3D GRF exhibits the highest similarity to the real structure, with a MAPE of only 0.00274.

Table 1. RVE structures generated by different Gaussian kernel widths.

SEM image	Width	$\sigma_1 = 1.5$	$\sigma_2 = 2.0$	$\sigma_3 = 2.5$	$\sigma_4 = 3.0$
The original image	GRF model				
Denoising & binarization	RVE				
Porosity：0.1867	MAPE	0.006567	0.004619	0.002929	0.003203

Fig. 8. RVE structure based on 3D GRF. (a) Normalized IAFs for different RVE structures and the real morphology. (b) Comparison of the RVE with the optimal Gaussian kernel width and the real morphology.

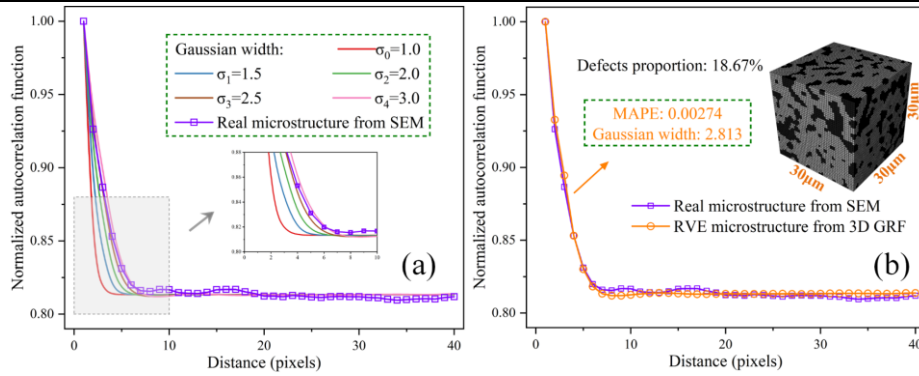Generally, it is difficult to obtain a complete constitutive curve for solid non-porous sintered AgNPs, as this material is essentially the aggregation of silver particles. This work uses the material properties of bulk pure Ag combined with homogenization methods to calculate the elastoplastic response of porous Ag (which has defect structures similar to sintered AgNPs as shown in Fig. 8(b)), as an approximation of the material properties of sintered AgNPs. The model parameters of the RVE are listed in Table 2, where the solid phase's performance curve is proposed by Huo et al. [40], the mesh failure displacement is calculated by Eq. (18). By maintaining the PBCs and applying further loads, the elastoplastic response of porous Ag can be obtained, as presented in Table 3 and Fig. 9.

$$U_f = L_0(\varepsilon_0^{pl} + \frac{1}{1-\psi} - 1) \tag{18}$$

Where U_f is the failure displacement. L_0 is the minimum mesh size. ε_0^{pl} the damage initiation strain of the ductile metal. ψ is the area shrinkage ratio (usually 0.5).

Table 2. Material parameters of RVE structure in ABAQUS.

Property	Categorization	Value	Unit
Elastic modulus	Solid phase	6344	MPa
	Defect phase	6.344	MPa
Poisson's ratio	Solid phase	0.37	/
	Defect phase	0.37	/
Density	Solid phase	7.50×10^3	kg/m³
	Defect phase	7.50×10^3	kg/m³
Yield strength	Solid phase	60	MPa
	Defect phase	6	MPa
Maximum tensile strength	Solid phase	133.5	MPa
	Defect phase	1.335	MPa
Damage initiation strain	Solid phase	0.21	/
	Defect phase	0.21	/
Mesh failure displacement	Solid phase	0.7235	μm
	Defect phase	0.7235	μm
RVE mesh size	0.6um×0.6um×0.6um		/

Table 3. Mechanical parameters of the sintered specimen predicted by RVE homogenization method.

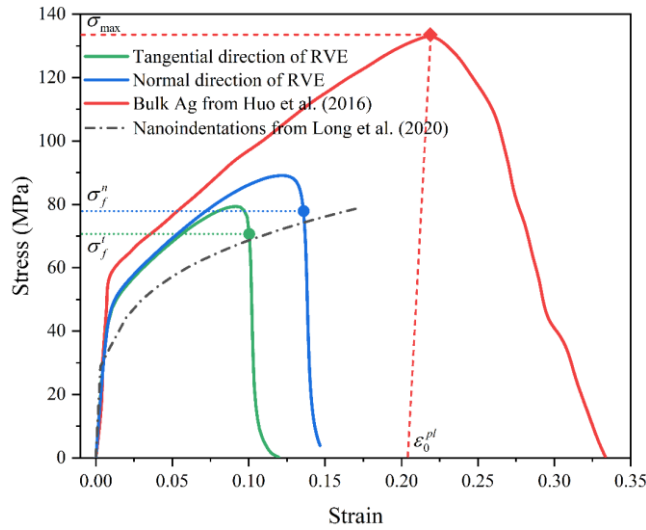| Young's modulus	Value	Poisson's ratio	Value
E_{11}	3733.54MPa	v_{12}	0.30
E_{22}	3847.32MPa	v_{13}	0.31
E_{33}	3732.25MPa	v_{21}	0.31
G_{12}	1404.26MPa	v_{23}	0.31
G_{13}	1387.50MPa	v_{31}	0.31
G_{23}	1385.27MPa	v_{32}	0.30

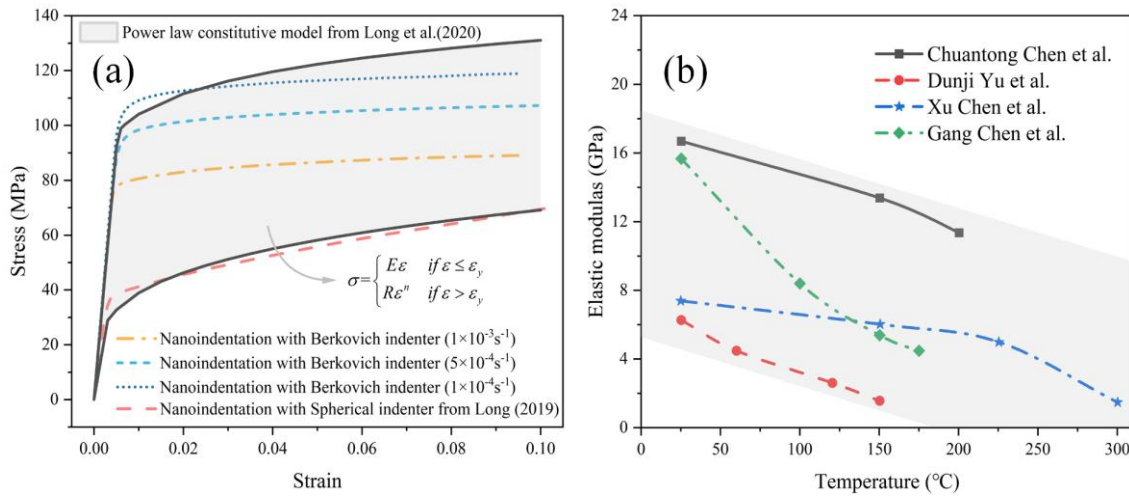Fig. 9. Normal and tangential elastoplastic responses of porous Ag

Fig. 10. The statistical analysis of sintering AgNPs material performance. (a) Measured by nanoindentation method. [41], [42], [43], (b) The elastic modulus' statistical results with different temperatures [44], [45], [46], [47].

The nanoindentation measurement data from Fig. 9 (black dashed line) [41] and the various strain rate and indenter configurations in Fig. 10 (a) indicate that the normal and tangential elastoplastic responses of porous silver, simulated using the RVE homogenization method, align with the power-law constitutive behavior of sintered AgNPs observed experimentally. Additionally, the mechanical property values, including yield stress and ultimate stress, also fall within the range of the measured data (gray area in Fig. 10(a)), further validating the effectiveness of the simulation results. Furthermore, the statistical results presented in Fig. 10(b) reveal an inverse relationship between the elastic modulus of sintered AgNPs and temperature. Thus, although the predicted elastic modulus at room temperature is numerically lower than the measured result, it is very close to the range of the measured data (gray area in Fig. 10(b)), which is acceptable from

a numerical standpoint. Therefore, the mechanical response curves of porous silver, obtained using the proposed method in this paper, are shown to be similar to those of sintered AgNPs.

Subsequently, the parameters for the cohesive elements corresponding to sintered AgNPs are calculated as follows: the maximum traction stress in the normal and tangential directions is determined using the σ_f^n and σ_f^s from Fig. 9 in conjunction with Eq. (15). when the cohesive element's calculated thickness is set to 1 mm, the elastic modulus obtained from Fig. 9 is equal to the stiffness. Based on these two parameters, the normal and tangential fracture energies are further calculated according to Eq. (16). At the same time, the cohesive element size l_e needs to be determined according to the length of the cohesive zone L_{cz}, which is defined as the distance from the crack tip to the point where the maximum cohesive traction is attained [48]. Moes and Belytschko [49], based on the work of Carpinteri et al. [50]

suggest that the L_{cz} typically needs to contain at least 10 cohesive elements to ensure both accuracy and convergence. So, the recommended range for l_e is calculated using Eq. (19) [51].

$$l_e = \frac{L_{cz}}{N_e} = \frac{2}{3\pi}\frac{EG_c/(\tau^0)^2}{N_e} = \frac{2EG_c}{3\pi N_e(\tau^0)^2} \in [0.079mm, 0.159mm] \quad (19)$$

Where E is elastic modulus. G_c is fracture energy. τ^0 is the interface stress, which is equal to the maximum traction. N_e is the number of units contained in the cohesive zone, ranging from 10 to 20.

Table 4. Cohesive element parameters of the sintered specimen in ABAQUS VUMT.

Parameters	Categorization	Value	Unit
Stiffness	normal direction: k_n	3847.32	MPa
	tangential direction: k_t	3733.55	MPa
Maximum traction stress	normal direction: f_{max_n}	105.15	MPa
	tangential direction: f_{max_t}	95.43	MPa
Fracture energy	normal direction: Gic	21.55	N/m
	tangential direction: $Gicc$	18.29	N/m
Density	/	7.50×10³	kg/m³
Cohesive element size	$l_e \in [0.079, 0.159]$	0.1	mm

Parameters	Categorization	Value	Unit
Cohesive elements calculate thickness.	$h_{thickness}$	1	mm
Characteristic parameters in new CCZM	a	1.2	/
	n	5	/
	C_f	0	/
	ne	0.2	/

Moreover, the characteristic parameters in the new CCZM are the suggested values presented in this paper, which will require adjustment for different materials and service environments in future applications. The cohesive element parameters for sintered AgNPs required in VUMAT are provided in Table 4.

4.3. Model verification and effect analysis

Both the simulation and verification experiments utilized the same periodic constant-amplitude loading conditions, with a maximum tensile displacement of 0.2 mm and a loading rate of 1.2 mm/min.
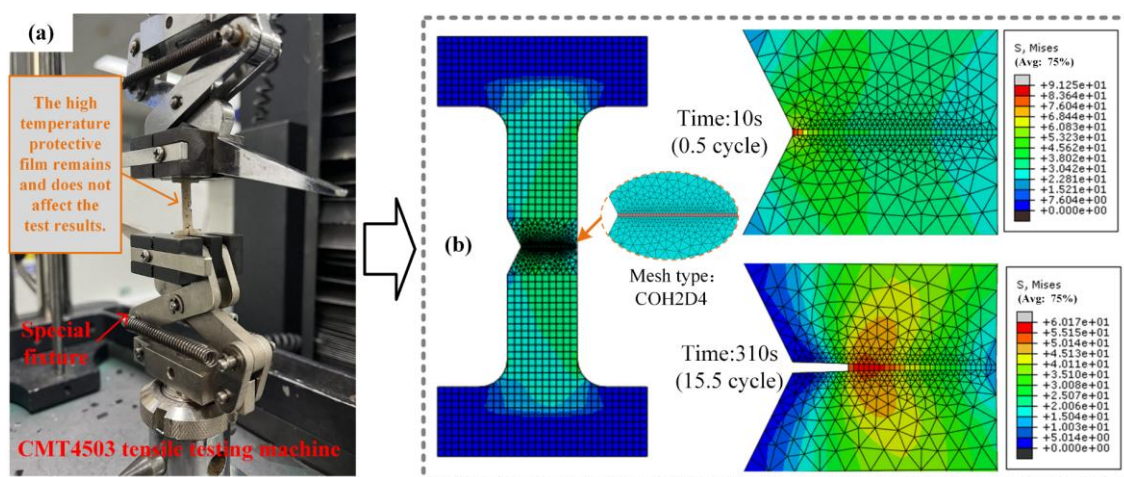

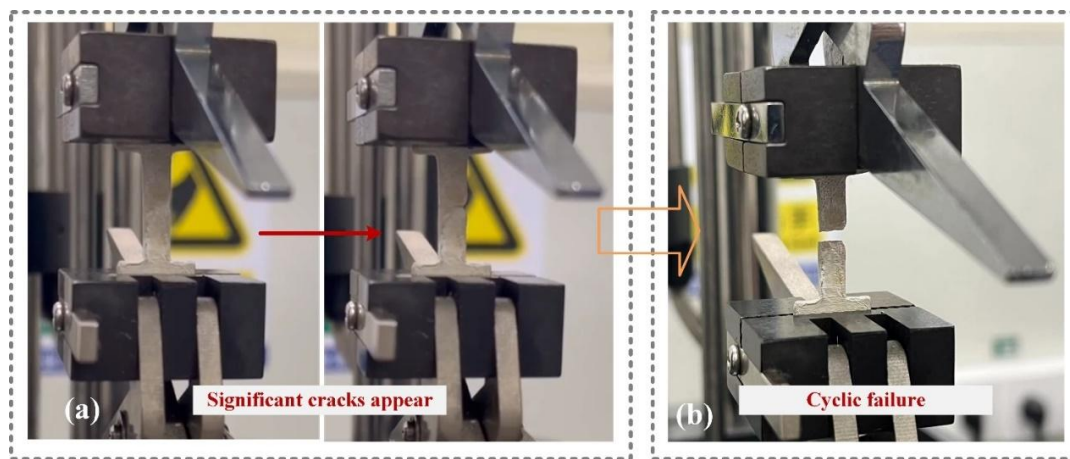Fig. 11. Cyclic loading tensile test and numerical simulation of sintered AgNPs.

Fig. 12. Failure process of sintered specimens under cyclic loading. (a) Significant crack growth phenomenon. (b) Fatigue fracture failure.
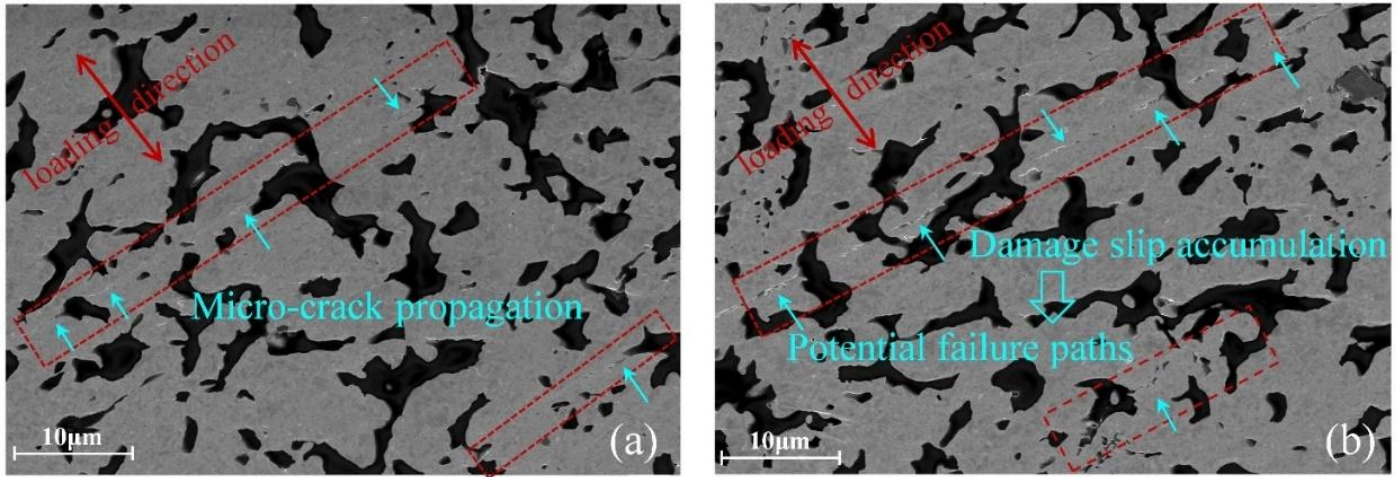
Fig. 13. SEM image of sintered specimen. (a) Micro-crack propagation in the early and middle stages of cyclic stretching. (b) Potential failure paths in other non-central fracture areas after failure.

The experimental and numerical simulation processes are shown in Fig. 11. Fig. 12 shows the failure process of the sintered specimen from a macroscopic perspective. Fig. 13 shows the micro-cracks propagation (early and middle stages of tension) and the potential failure paths that appear in the non-fracture area (final stages of fatigue failure). These confirm that the accumulation of damage slip occurs inside the sintered AgNPs and gradually develops into a potential crack propagation path as the number of cycles increases. Furthermore, it should be clarified that the new CCZM proposed in this paper aims primarily to provide a solution that balances model complexity and engineering convenience for predicting the lifetime of sintered AgNPs, rather than offering

a detailed simulation of crack propagation. The internal fatigue degradation behavior of these materials is reflected by the damage value of a cohesive element. Fig.14 shows the effect of different values of l_e with the recommended size range on the model's tensile stress and failure cycle count. It can be observed that the value of l_e chosen as 0.1mm in this study satisfies both computational efficiency and accuracy requirements. Fig. 15 (a) shows the comparison between the simulation results and experimental data. Although the new CCZM predicts a slightly conservative estimate of failure cycles compared to the experimental average, it remains within an acceptable range. Therefore, the new CCZM is deemed suitable for sintered AgNPs' fatigue prediction.
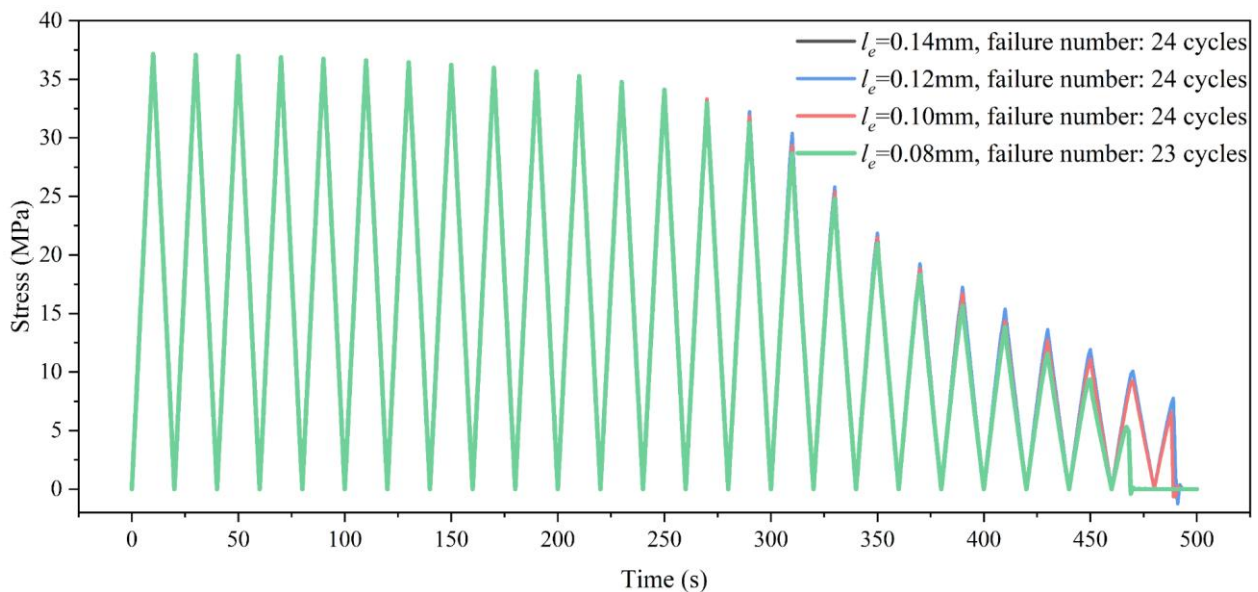

Fig. 14. The effect of different cohesive element sizes on the simulation results.
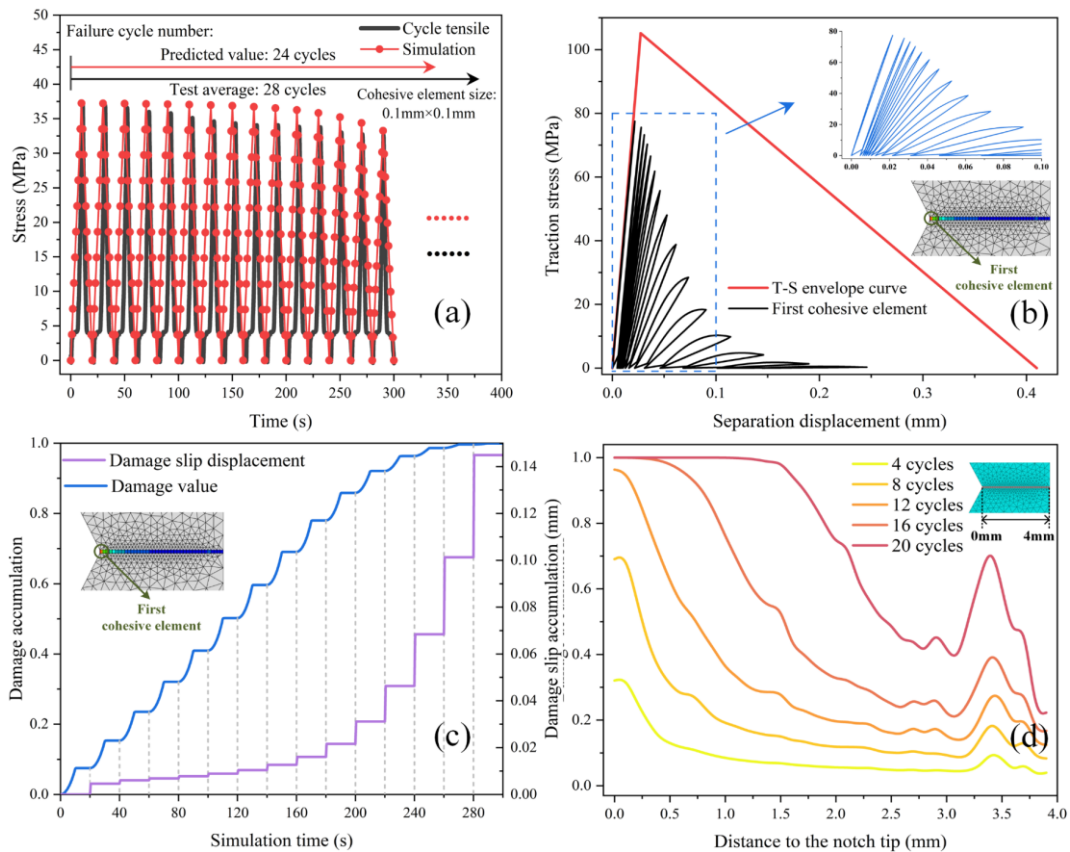
Fig. 15. Simulation effect of the new CCZM. (a) Comparison between experiment and simulation. (b) T-S curve of the first cohesive element under the cyclic loading test. (c) Fatigue damage results and the damage slip accumulation of the first cohesive element. (d) The damage evolution of cohesive elements with different cycle numbers.

Fig. 15(b) shows the T-S curve of the first cohesive element under cyclic loading. Fig. 15(c) presents the fatigue damage results and the accumulation of damage slip in the first cohesive element. Minor damage occurs even with tensile stress below f_{max}. Moreover, the cumulative impact of damage slip becomes increasingly apparent during cyclic loading. On one hand, the accumulation of fatigue damage leads to porous structural deterioration in sintered AgNPs. The virtual connection part will not hinder crack propagation when stress reloading. At this stage, the cohesive element will start moving from the position of accumulated damage slip. Additionally, damage slip alters the model's stress distribution under loading, influencing the crack propagation process. On the other hand, the gradual accumulation of damage slip shifts the T-S curve rightward, approaching the envelope curve and resulting in monotonic damage. These phenomena are more pronounced under low-stress cyclic loading.

Fig. 15(d) shows the damage evolution of cohesive elements with different cycle numbers. The analysis reveals that the cohesive elements remain in the damage accumulation stage during the first 12 cycles. Significant crack propagation and increasing growth rate are observed during 12~20 cycles, leading to a 1.5 mm crack length. In addition to the damage observed at the front of the cohesive zone, noticeable damage also occurs at the tail. This is because the model has a preset notch of 1 mm. During the simulation, the stress on the right side of the cohesive zone is not concentrated at the edge cohesive element but rather near the symmetric position of the left-side notch, due to the symmetry of the model. The position primarily depends on the preset notch shape, model shape, and stress loading mode. Moreover, according to the damage calculation rule of the new CCZM, an increase in stress leads to a more pronounced reduction in the stiffness and strength of the cohesive elements, resulting in a significant damage slip phenomenon. According to the constitutive rules defined in this study, this process is also interactive, resulting in significant damage accumulation at the 3.3 mm position after multiple cycles.

So far, the above case analyzes have proved the accuracy and effectiveness of the new CCZM in fatigue life prediction.

5. Characteristic parameter sensitivity analysis

Characteristic parameter changes in the new CCZM significantly affect the crack growth process and lifetime prediction results, making it necessary to analyze their influence. Fig. 16 shows the effect of model characteristic parameters and stretching rate on crack mouth opening displacement (CMOD). Elevating parameters a and ne increases the crack growth rate, whereas an increase in C_f reduces damage accumulation and retards crack growth. Notably, despite the influence of parameters a and C_f on crack growth rates, three typical stages of crack propagation—crack initiation, crack growth, and rapid fracture—can still be clearly distinguished. However, the increase in ne linked to damage slip will make the crack initiation stage less obvious, leading swiftly to the crack growth stage. Additionally, when the cycle period is fixed, a higher tensile rate results in larger loading displacements and traction stress, which leads to more pronounced reductions in the

stiffness and strength of the cohesive elements, as well as larger damage slip values. After multiple cycles, the effects of fatigue damage and slip accumulation become more significant, which means the cohesive mesh will fail more rapidly, leading to an increase in the crack growth rate, as shown in Fig. 16(d).

Fig. 17 shows the effect of model parameters and stretching rate on fatigue lifetime. An increase in a from a_0 to $1.8a_0$, reduces the fatigue lifetime by an average of 32.63%. When C_f increases from C_{f0} to $20C_{f0}$, the fatigue lifetime increases by an average of 10.92% on average. Increasing ne from ne_0 to $20ne_0$ decreases the fatigue lifetime by an average of 12.44%. Considering the magnification value, the fatigue lifetime is more sensitive to the parameter a. In addition, when the cycle period is fixed, increasing the stretching rate v by 1.8 times is equivalent to a 1.8-fold increase in the loading displacement per cycle, the fatigue lifetime decreases by 54.35% on average. Thus, the sensitive factor of stretching rate also cannot be ignored.
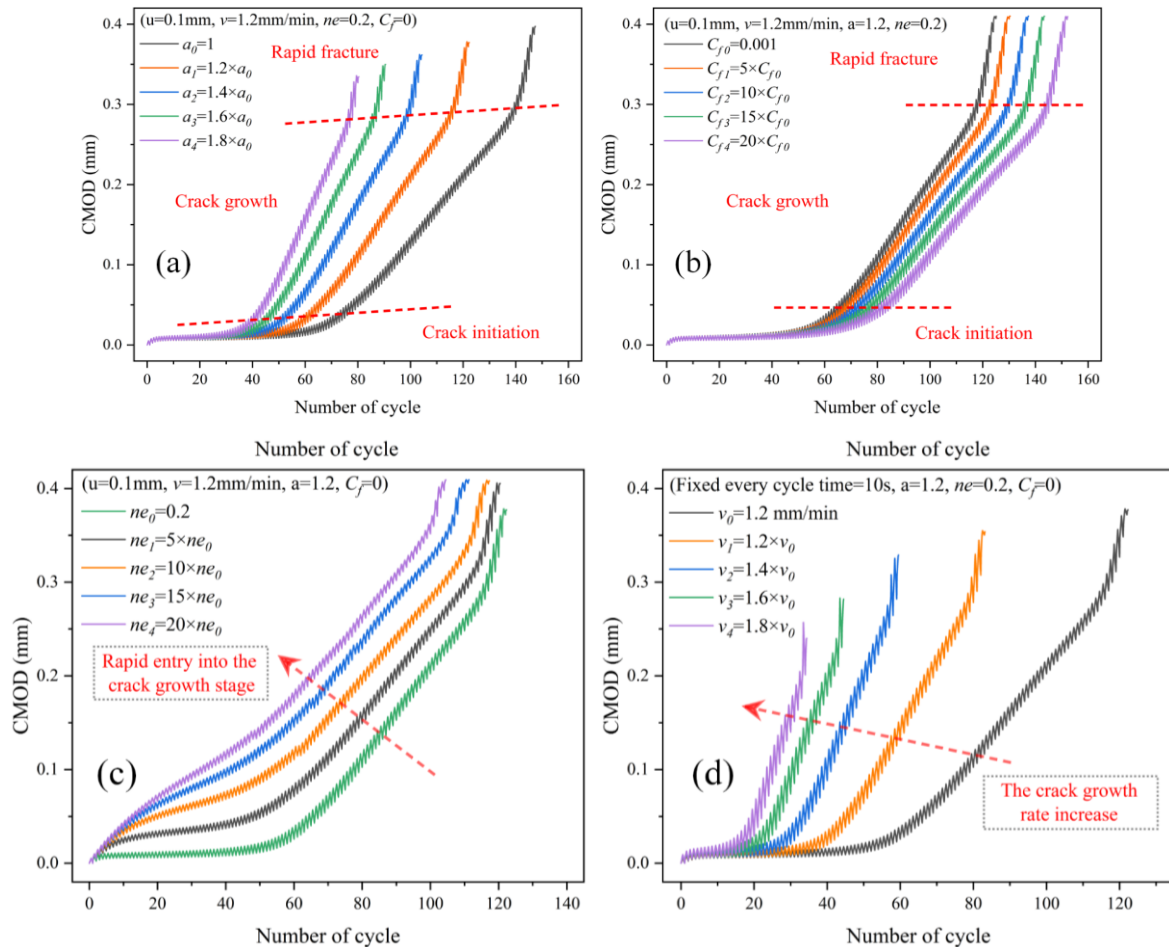

Fig. 16. The effect of model characteristic parameters and stretching rate on CMOD. (a) CMOD affected by parameter a. (b) CMOD affected by parameter Cf. (c) CMOD affected by parameter ne. (d) CMOD affected by parameter v (each cycle period is 10s, with 5s for loading and 5s for unloading).
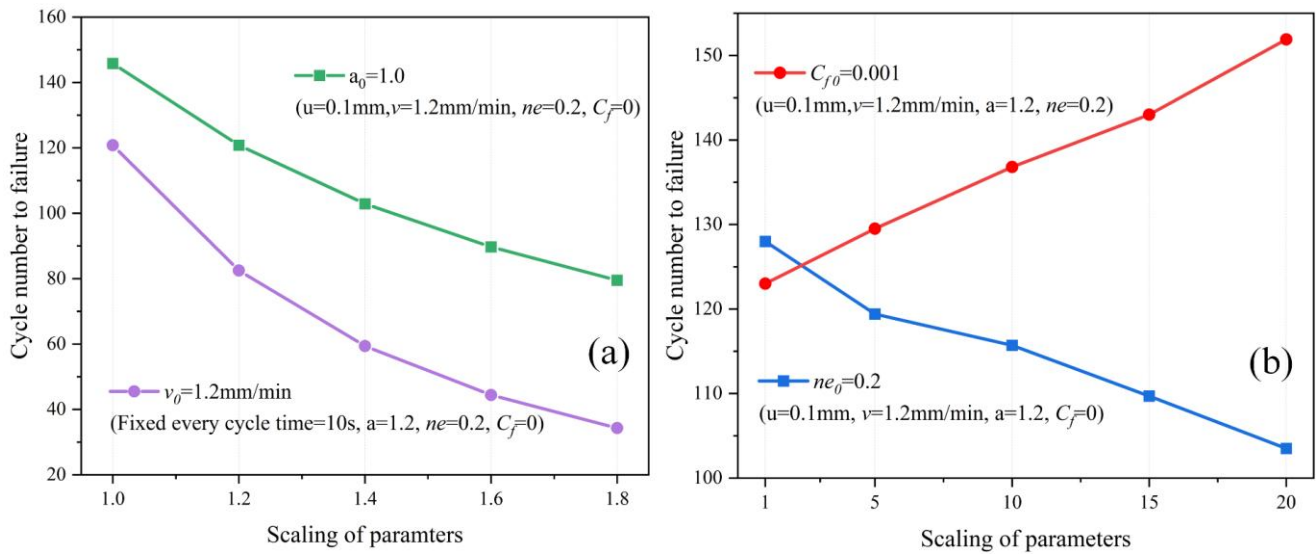
Fig. 17. The effect of model characteristic parameters and stretching rate on fatigue lifetime. (a) Fatigue lifetime affected by parameter a and v. (b) Fatigue lifetime affected by parameter Cf. and ne

6. Conclusion

In this work, a new CCZM for predicting the fatigue lifetime of sintered AgNPs is proposed. The conclusions can be summarized as follows:

1) This fatigue model uniquely accounts for both damage slip accumulation and simultaneous degradation of stiffness and strength. This approach avoids the unrealistic assumption that porous structures remain perpetually in the elastic stage under low stresses.

2) The detailed application of the new CCZM is presented, including a cost-effective method for estimating key model parameters, and the development of a VUMAT user subroutine for the ABAQUS explicit solver

3) The effectiveness of the new CCZM in lifetime prediction was verified by cyclic tensile tests on sintered specimens, and the existence of damage slip phenomena was confirmed. Moreover, a comprehensive analysis and discussion of the sensitivity of the model's characteristic parameters was conducted with particular focus on their influence on the three typical stages of crack propagation. It was also found that the lifetime prediction results are more sensitive to the model's characteristic parameter a.

4) This paper presents a novel method for predicting the service lifetime of sintered AgNPs and offers a fresh perspective on the reliability analysis of porous structures, thereby assisting in their reliable application within packaging interconnect structures.

References

1. S. A. Paknejad and S. H. Mannan, "Review of silver nanoparticle based die attach materials for high power/temperature applications," *Microelectronics Reliability*, vol. 70, pp. 1–11, Mar. 2017, doi: 10.1016/j.microrel.2017.01.010.

2. J. Wang, S. Chen, L. Zhang, X. Zhao, F. Duan, and H. Chen, "Brief Review of Nanosilver Sintering: Manufacturing and Reliability," *J. Electron. Mater.*, vol. 50, no. 10, pp. 5483–5498, Oct. 2021, doi: 10.1007/s11664-021-09078-1.

3. Y. Su, G. Fu, C. Liu, C. Liu, and X. Long, "Fatigue crack evolution and effect analysis of Ag sintering die-attachment in SiC power devices under power cycling based on phase-field simulation," *Microelectronics Reliability*, vol. 126, p. 114244, Nov. 2021, doi: 10.1016/j.microrel.2021.114244.

4. J. H. Lau, "Recent Advances and Trends in Chiplet Design and Heterogeneous Integration Packaging," *Journal of Electronic Packaging*, vol. 146, no. 010801, Jun. 2023, doi: 10.1115/1.4062529.

5. Y. Wang *et al.*, "Research on the Reliability of Advanced Packaging under Multi-Field Coupling: A Review," *Micromachines*, vol. 15, no. 4, Art. no. 4, Apr. 2024, doi: 10.3390/mi15040422.

6. X. Zhan, Z. Liu, H. Yan, Z. Wu, C. Guo, and X. Jia, "A novel method of health indicator construction and remaining useful life prediction

based on deep learning," *Eksploatacja i Niezawodność – Maintenance and Reliability*, vol. 25, no. 4, Aug. 2023, doi: 10.17531/ein/171374.

7.   D. Liu and S. Wang, "Reliability estimation from lifetime testing data and degradation testing data with measurement error based on evidential variable and Wiener process," *Reliability Engineering & System Safety*, vol. 205, p. 107231, Jan. 2021, doi: 10.1016/j.ress.2020.107231.

8.   C. Mi, Y. Xiao, Y. Deng, and Y. Li, "Fatigue Life Prediction of LF6 Aluminum Alloy Laser-Arc Hybrid Welded Joints Based on Energy Dissipation Method," *Fatigue & Fracture of Engineering Materials & Structures*, vol. 2024, no. 0, pp. 1–13, Nov. 2024, doi: 10.1111/ffe.14517.

9.   C. Mi, W. Liu, C. Wen, Y. Tang, J. Wu, and G. Risitano, "Fatigue failure analysis and lifetime prediction of self-piercing riveted dissimilar aluminum alloy joint based on energy method," *Engineering Failure Analysis*, vol. 165, p. 108746, Nov. 2024, doi: 10.1016/j.engfailanal.2024.108746.

10.   M. Modarres, "Probabilistic Physics of Failure Concept and Its Application in Reliability Engineering," *IEEE Transactions on Reliability*, vol. 73, no. 1, pp. 19–20, Mar. 2024, doi: 10.1109/TR.2024.3357811.

11.   Y. Murakami, T. Takagi, K. Wada, and H. Matsunaga, "Essential structure of *S-N* curve: Prediction of fatigue life and fatigue limit of defective materials and nature of scatter," *International Journal of Fatigue*, vol. 146, p. 106138, May 2021, doi: 10.1016/j.ijfatigue.2020.106138.

12.   T. Amla and N. Chawla, "Finite Element Method Analysis of Fatigue and Damage in Low-Temperature-Sintered Nano-silver Soldered Joints," *J. Electron. Mater.*, vol. 52, no. 2, pp. 760–772, Feb. 2023, doi: 10.1007/s11664-022-10097-9.

13.   J. Heilmann, B. Wunderle, U. Zschenderlein, C. Wille, and K. Pressel, "Physics of failure based lifetime modelling for sintered silver die attach in power electronics: Accelerated stress testing by isothermal bending and thermal shock in comparison," *Microelectronics Reliability*, vol. 145, p. 114973, Jun. 2023, doi: 10.1016/j.microrel.2023.114973.

14.   S. M. Zaharia, "The methodology of fatigue lifetime prediction and validation based on accelerated reliability testing of the rotor pitch links," *Eksploatacja i Niezawodnosc-Maintenance and Reliability*, vol. 21, no. 4, pp. 638–644, Dec. 2019, doi: 10.17531/ein.2019.4.13.

15.   Y. Liu, Y. Wang, Z. Fan, Z. Hou, S. Zhang, and X. Chen, "Lifetime prediction method for MEMS gyroscope based on accelerated degradation test and acceleration factor model," *Eksploatacja i Niezawodność – Maintenance and Reliability*, vol. 22, no. 2, pp. 221–231, Jun. 2020, doi: 10.17531/ein.2020.2.5.

16.   A. Chudzik and B. Warda, "Fatigue life prediction of a radial cylindrical roller bearing subjected to a combined load using FEM," *Eksploatacja i Niezawodność – Maintenance and Reliability*, vol. 22, no. 2, pp. 212–220, Jun. 2020, doi: 10.17531/ein.2020.2.4.

17.   M. Kuna and S. Roth, "General remarks on cyclic cohesive zone models," *Int J Fract*, vol. 196, no. 1, pp. 147–167, Nov. 2015, doi: 10.1007/s10704-015-0053-y.

18.   H. Yuan and X. Li, "Critical remarks to cohesive zone modeling for three-dimensional elastoplastic fatigue crack propagation," *Engineering Fracture Mechanics*, vol. 202, pp. 311–331, Oct. 2018, doi: 10.1016/j.engfracmech.2018.03.018.

19.   Y.-H. Choi and H.-G. Kim, "Development of a Cohesive Zone Model for Fatigue Crack Growth," *Multiscale Sci. Eng.*, vol. 2, no. 1, pp. 42–53, Mar. 2020, doi: 10.1007/s42493-020-00034-5.

20.   M. Kuna and S. Roth, "General remarks on cyclic cohesive zone models," *Int J Fract*, vol. 196, no. 1, pp. 147–167, Nov. 2015, doi: 10.1007/s10704-015-0053-y.

21.   X. Xi, S. Yang, C. I. McDermott, Z. K. Shipton, A. Fraser-Harris, and K. Edlmann, "Modelling Rock Fracture Induced By Hydraulic Pulses," *Rock Mech Rock Eng*, vol. 54, no. 8, pp. 3977–3994, Aug. 2021, doi: 10.1007/s00603-021-02477-0.

22.   K. L. Roe and T. Siegmund, "An irreversible cohesive zone model for interface fatigue crack growth simulation," *Engineering Fracture Mechanics*, vol. 70, no. 2, pp. 209–232, Jan. 2003, doi: 10.1016/S0013-7944(02)00034-6.

23.   S. Maiti and P. H. Geubelle, "A cohesive model for fatigue failure of polymers," *Engineering Fracture Mechanics*, vol. 72, no. 5, pp. 691–708, Mar. 2005, doi: 10.1016/j.engfracmech.2004.06.005.

24.   R. Wang, Y. Liu, J. Mao, Z. Liu, and D. Hu, "Cyclic cohesive zone model damage parameter acquisition for fatigue crack growth considering crack closure effect," *International Journal of Fatigue*, vol. 163, p. 107021, Oct. 2022, doi: 10.1016/j.ijfatigue.2022.107021.

25.   S. Roth, G. Hütter, and M. Kuna, "Simulation of fatigue crack growth with a cyclic cohesive zone model," *Int J Fract*, vol. 188, no. 1, pp. 23–45, Jul. 2014, doi: 10.1007/s10704-014-9942-8.

26. S. Roth and M. Kuna, "Prediction of size-dependent fatigue failure modes by means of a cyclic cohesive zone model," *International Journal of Fatigue*, vol. 100, pp. 58–67, Jul. 2017, doi: 10.1016/j.ijfatigue.2017.01.044.

27. A. Skar, P. N. Poulsen, and J. F. Olesen, "General cracked-hinge model for simulation of low-cycle damage in cemented beams on soil," *Engineering Fracture Mechanics*, vol. 175, pp. 324–338, Apr. 2017, doi: 10.1016/j.engfracmech.2017.01.016.

28. X. Xi and S. Yang, "A non-linear cohesive zone model for low-cycle fatigue of quasi-brittle materials," *Theoretical and Applied Fracture Mechanics*, vol. 122, p. 103641, Dec. 2022, doi: 10.1016/j.tafmec.2022.103641.

29. F. Hosseinabadi, S. Chakraborty, S. K. Bhoi, G. Prochart, D. Hrvanovic, and O. Hegazy, "A Comprehensive Overview of Reliability Assessment Strategies and Testing of Power Electronics Converters," *IEEE Open Journal of Power Electronics*, vol. 5, pp. 473–512, 2024, doi: 10.1109/OJPEL.2024.3379294.

30. Z. Zhang *et al.*, "Impact Analysis of Microscopic Defect Types on the Macroscopic Crack Propagation in Sintered Silver Nanoparticles," *CMES*, vol. 139, no. 1, pp. 441–458, 2023, doi: 10.32604/cmes.2023.043616.

31. H. Mughrabi, "Cyclic Slip Irreversibilities and the Evolution of Fatigue Damage," *Metall Mater Trans B*, vol. 40, no. 4, pp. 431–453, Aug. 2009, doi: 10.1007/s11663-009-9240-4.

32. C. Chen *et al.*, "Self-healing of cracks in Ag joining layer for die-attachment in power devices," *Applied Physics Letters*, vol. 109, no. 9, p. 093503, Sep. 2016, doi: 10.1063/1.4962333.

33. Y. Su, Z. Shen, X. Long, C. Chen, L. Qi, and X. Chao, "Gaussian filtering method of evaluating the elastic/elasto-plastic properties of sintered nanocomposites with quasi-continuous volume distribution," *Materials Science and Engineering: A*, vol. 872, p. 145001, May 2023, doi: 10.1016/j.msea.2023.145001.

34. R. Hill, "Elastic properties of reinforced solids: Some theoretical principles," *Journal of the Mechanics and Physics of Solids*, vol. 11, no. 5, pp. 357–372, Sep. 1963, doi: 10.1016/0022-5096(63)90036-X.

35. Z. Xia, Y. Zhang, and F. Ellyin, "A unified periodical boundary conditions for representative volume elements of composites and applications," *International Journal of Solids and Structures*, vol. 40, no. 8, pp. 1907–1921, Apr. 2003, doi: 10.1016/S0020-7683(03)00024-6.

36. S. L. Omairey, P. D. Dunning, and S. Sriramula, "Development of an ABAQUS plugin tool for periodic RVE homogenisation," *Engineering with Computers*, vol. 35, no. 2, pp. 567–577, Apr. 2019, doi: 10.1007/s00366-018-0616-4.

37. Y. J. Wang and C. Q. Ru, "Determination of two key parameters of a cohesive zone model for pipeline steels based on uniaxial stress-strain curve," *Engineering Fracture Mechanics*, vol. 163, pp. 55–65, Sep. 2016, doi: 10.1016/j.engfracmech.2016.06.017.

38. K. Kendall, "New theory explaining Griffith strength results on nano-cracked glass fibres," *Philosophical Transactions of the Royal Society A: Mathematical, Physical and Engineering Sciences*, vol. 380, no. 2232, p. 20210348, Aug. 2022, doi: 10.1098/rsta.2021.0348.

39. Y. Dai, Y. Li, Z. Zan, and F. Qin, "Bondline thickness effect on fracture and cohesive zone model of sintered nano silver adhesive joints under end notched flexure tests," *Fatigue & Fracture of Engineering Materials & Structures*, vol. 46, no. 6, pp. 2062–2079, 2023, doi: 10.1111/ffe.13981.

40. Y. Huo and C. C. Lee, "The growth and stress vs. strain characterization of the silver solid solution phase with indium," *Journal of Alloys and Compounds*, vol. 661, pp. 372–379, Mar. 2016, doi: 10.1016/j.jallcom.2015.11.212.

41. X. Long, Q. P. Jia, Z. Li, and S. X. Wen, "Reverse analysis of constitutive properties of sintered silver particles from nanoindentations," *International Journal of Solids and Structures*, vol. 191–192, pp. 351–362, May 2020, doi: 10.1016/j.ijsolstr.2020.01.014.

42. X. Long, Q. Jia, Z. Shen, M. Liu, and C. Guan, "Strain rate shift for constitutive behaviour of sintered silver nanoparticles under nanoindentation," *Mechanics of Materials*, vol. 158, p. 103881, Jul. 2021, doi: 10.1016/j.mechmat.2021.103881.

43. X. Long *et al.*, "Mechanical behaviour of sintered silver nanoparticles reinforced by SiC microparticles," *Materials Science and Engineering: A*, vol. 744, pp. 406–414, Jan. 2019, doi: 10.1016/j.msea.2018.12.015.

44. D. Yu, X. Chen, G. Chen, G. Lu, and Z. Wang, "Applying Anand model to low-temperature sintered nanoscale silver paste chip attachment," *Materials & Design*, vol. 30, no. 10, pp. 4574–4579, Dec. 2009, doi: 10.1016/j.matdes.2009.04.006.

45. C. Chen, C. Choe, D. Kim, and K. Suganuma, "Lifetime Prediction of a SiC Power Module by Micron/Submicron Ag Sinter Joining Based on Fatigue, Creep and Thermal Properties from Room Temperature to High Temperature," *J. Electron. Mater.*, vol. 50, no. 3, pp. 687–698, Mar. 2021, doi: 10.1007/s11664-020-08410-5.

46. X. Chen, R. Li, K. Qi, and G.-Q. Lu, "Tensile Behaviors and Ratcheting Effects of Partially Sintered Chip-Attachment Films of a Nanoscale Silver Paste," *J. Electron. Mater.*, vol. 37, no. 10, pp. 1574–1579, Oct. 2008, doi: 10.1007/s11664-008-0516-2.

47. G. Chen and X. Zhao, "Constitutive modelling on the whole-life uniaxial ratcheting behavior of sintered nano-scale silver paste at room and high temperatures," *Microelectronics Reliability*, vol. 80, pp. 47–54, Jan. 2018, doi: 10.1016/j.microrel.2017.11.010.

48. A. Turon, C. G. Dávila, P. P. Camanho, and J. Costa, "An engineering solution for mesh size effects in the simulation of delamination using cohesive zone models," *Engineering Fracture Mechanics*, vol. 74, no. 10, pp. 1665–1682, Jul. 2007, doi: 10.1016/j.engfracmech.2006.08.025.

49. N. Moës and T. Belytschko, "Extended finite element method for cohesive crack growth," *Engineering Fracture Mechanics*, vol. 69, no. 7, pp. 813–833, May 2002, doi: 10.1016/S0013-7944(01)00128-X.

50. A. Carpinteri, P. Cornetti, F. Barpi, and S. Valente, "Cohesive crack model description of ductile to brittle size-scale transition: dimensional analysis vs. renormalization group theory," *Engineering Fracture Mechanics*, vol. 70, no. 14, pp. 1809–1839, Sep. 2003, doi: 10.1016/S0013-7944(03)00126-7.

51. C.-Y. Hui, J. A, S. J. Bennison, and J. D. Londono, "Crack blunting and the strength of soft elastic solids," *Proc. R. Soc. Lond. A*, vol. 495, pp. 1489–1516, Jun. 2003, doi: 10.1098/rspa.2002.1057.